Cotterell, M. I., Mason, B. J., Carruthers, A. E., Walker, J. S., Orr-Ewing, A. J., & Reid, J. P. (2014). Measurements of the evaporation and hygroscopic response of single fine-mode aerosol particles using a Bessel beam optical trap. *Physical Chemistry Chemical Physics*, *16*(5), 2118-2128. https://doi.org/10.1039/c3cp54368d

Measurements of the Evaporation and Hygroscopic Response of Single Fine-Mode Aerosol Particles Using a Bessel Beam Optical Trap

Michael I. Cotterell,[1] Bernard J. Mason,[1] Antonia E. Carruthers,[2] Jim S. Walker,[1] Andrew J. Orr-Ewing[1] and Jonathan P. Reid[1]

[1] School of Chemistry, University of Bristol, Bristol, UK BS8 1TS

[2] School of Chemistry, Newcastle University, Newcastle Upon Tyne, UK NE1 7RU

A single horizontally-propagating zeroth order Bessel laser beam with a counter-propagating gas flow was used to confine single fine-mode aerosol particles over extended periods of time, during which process measurements were performed. Particle sizes were measured by the analysis of the angular variation of light scattered at 532 nm by a particle in the Bessel beam, using either a probe beam at 405 nm or 633 nm. The vapour pressures of glycerol and 1,2,6-hexanetriol particles were determined to be 7.5±2.6 mPa and 0.20±0.02 mPa respectively. The lower volatility of hexanetriol allowed better definition of the trapping environment relative humidity profile over the measurement time period, thus higher precision measurements were obtained compared to those for glycerol. The size evolution of a hexanetriol particle, as well as its refractive index at wavelengths 532 nm and 405 nm, were determined by modelling its position along the Bessel beam propagation length while collecting phase functions with the 405 nm probe beam. Measurements of the hygroscopic growth of sodium chloride and ammonium sulfate have been performed on particles as small as 350 nm in radius, with growth curves well described by widely used equilibrium state models. These are the smallest particles for which single-particle hygroscopicity has been measured and represent the first measurements of hygroscopicity on fine mode and near-accumulation mode aerosols, the size regimes bearing the most atmospheric relevance in terms of loading, light extinction and scattering. Finally, the technique is contrasted with other single particle and ensemble methods, and limitations are assessed.

I. Introduction

Atmospheric aerosols play important roles in regulating the Earth's climate and influencing atmospheric composition, as well as impacting on human health, yet many of the fundamental physicochemical properties of aerosol remain poorly understood and quantified.[1] As well as their ability to scatter solar radiation directly, atmospheric aerosols indirectly affect climate by providing cloud condensation nuclei (CCN) for cloud droplets, impacting on the size, composition and lifetime of clouds.[1,2] Understanding the condensational growth of an aerosol and the partitioning of water between the gas and particle phases is critical to describe accurately the size distribution and composition of atmospheric aerosol.[3] Measurements of the response of the equilibrium particle size and composition to changes in relative humidity (RH) can be used to quantify the hygroscopicity of the aerosol**,** the capacity of a particle to absorb water from the surrounding vapour.[4–7] Further, changes in the partitioning of volatile and semi-volatile solutes (organic and inorganic) between the particle and gas phases can accompany changes in the RH.[8] Measurements of the decreasing radius of a particle evaporating into a gas phase devoid of the volatile or semi-volatile component can allow the vapour pressure of the component to be determined.[9–11]

Ensemble measurements have been used extensively to probe aerosol systems in the fine (< 2.5 μm diameter) and accumulation (0.1 - 1 μm) mode regimes, providing measurements of quantities averaged over a large number of particles with insufficient resolution to quantify aerosol processes robustly at the fundamental level of individual particles. Single particle techniques can be employed successfully in the measurement of aerosol optical and thermodynamic properties, as well as their kinetic response, and have the potential to resolve the fundamental detail of physicochemical processes.[11] The use of electrodynamic balances (EDBs) to isolate and study single particles is well established, with recent improvements in experimental techniques allowing highly accurate measurements of particle hygroscopicity, but has been largely limited to studying coarse mode particles > 5 μm in radius.[9,4] Optical tweezers are routinely used to isolate and study aerosol particles 1 - 10 μm in radius, still much larger than the accumulation mode particles that are of direct atmospheric importance.[12,13,2,14] Thus, the size regimes examined by ensemble and single-particle

techniques do not overlap; there is a need for new techniques to control and characterise individual fine mode particles in order to reconcile single particle and ensemble measurements.

The need for single aerosol particle studies in the fine mode is augmented by the fact that some significant and atmospherically-relevant aerosol processes occur for diameters well below 1 micron. For example, the Kelvin equation shows that the vapour pressure for semi-volatile organic aerosol (SVOA) increases exponentially as the particle radius decreases (and the surface curvature increases).[15] However, the influence of the Kelvin effect is negligible for the coarse mode particles that are probed in existing single particle techniques. Although measurements of the kinetics of aerosol transformation (for example, heterogeneous oxidative aging or water condensation/ evaporation) can be made routinely on single coarse mode particles, the accuracy of scaling the observed kinetics to the much smaller fine mode particles found in the atmosphere is frequently debated.[11] Further, and of particular relevance for the direct influence of aerosol on climate, particle diameters in the range 500 nm to 1 μm are of sufficiently high number concentration and optical cross-section to play a significant role in atmospheric optics. Direct measurements of aerosol optical properties in this size range would be particularly advantageous. Single particle techniques that can access the fine mode and push the lower size limit down well into the accumulation mode would expand the range of particle sizes accessible to single particle techniques and allow the robust assessment and development of thermodynamic, kinetic and optical models.

A carefully engineered Bessel laser beam[16,17] may be used as an optical trap for single, as well as multiple, aerosol particles across a range of particle sizes, from 10s of microns to a few hundred nanometres in diameter.[18–20] The intensity profile along the transverse direction (*i.e.* in the direction perpendicular to the optical propagation axis) of a zeroth order Bessel beam (BB) is circularly symmetric with a central core of intensity surrounded by multiple rings. It can be shown by Fourier optics that such a beam is realisable by propagating the wave vectors of an incident beam along a cone, which may be achieved using a conical-shaped lens, or *axicon*.[21–24] The axicon method generates a BB over an extended distance due to the large region over which waves may interfere. If

an imaging plane is placed at any point along this interference region, a Bessel-squared intensity distribution is observed. Crucially, the core of a BB appears *non-diffracting* and retains its size and shape over a macroscopic length far larger than the characteristic Rayleigh range of a Gaussian beam with the same focal beam waist as the BB core diameter.[16] If a particle is irradiated by the core of a BB, it will experience radiation pressure force in the direction of the propagation axis of the beam, while optical gradient forces act in the transverse directions to retain the particle within the core. To confine single particles along the BB propagation length, the radiation pressure force needs to be balanced. If two counter-propagating BBs are used, a radiation pressure trap is created in which the trapping of both spherical and non-spherical sub-micron particles over macroscopic distances may be achieved.[18]

Previous work has shown that BBs can be used to trap and characterise multiple aerosol particles 500 to 2000 nm in radius, with their sizes resolved from the angular variation of elastically scattered light.[18,19] We have previously shown that the accuracy of such sizing methods can be enhanced by sizing with multiple-wavelength probe beams, which is particularly valuable for determinations of size for particles below 1 micron in radius. Furthermore, the size range of particles trapped by the beam can be coarsely tuned by varying the core size and laser power of the BB, and may be optimised for trapping fine mode particles. More recently, we have reported the use of a vertically propagating BB optical trap coupled with cavity ring-down spectroscopy to measure directly the optical extinction by single aerosol particles[20]

The purpose of this paper is to demonstrate that BBs can be used to study the physiochemical properties of fine mode aerosols over extended periods of time. A single horizontally propagating BB is coupled with a counter-propagating gas flow to balance the radiation pressure force exerted on confined aerosol particles. This arrangement allows the environment around a single particle to be varied easily without perturbing the trapping stability. Measurements of particle hygroscopicity and gas-particle partitioning of semi-volatile components are reported.

II. Experimental Description

The experimental apparatus used is summarised in Figure 1. A 532 nm Gaussian laser beam (Laser Quantum 3W Opus) was expanded using a pair of lenses (L1 and L2) to illuminate the back-aperture of a 2^{o} axicon (Altechna), generating a region of interference of approximately one meter in length over which a BB was formed. Immediately after the axicon, the BB core diameter was measured to be 55 μm, which is too large to trap sub-micron aerosols. Hence, a further pair of lenses (L3 and L4) was used to reduce the core diameter by a factor of 12.5 times to 4.7 ± 0.3 μm, propagating over a distance of approximately 5 mm. This beam was directed into the trapping cell. The radiation pressure exerted by this horizontally propagating BB on a trapped particle was balanced by a humidified nitrogen gas flow of 50 sccm, the RH of which could be controlled. This gas flow was also used to purge the cell of excess aerosol. The speed of the gas flow combined with the geometry of the trapping cell yields a Reynolds number *Re* close to 1, much lower than the critical value for *Re* of approximately 3000 for turbulent flow. The RH inside the trapping cell was monitored using a capacitance probe (Honeywell). A camera (C1) coupled to a 20× long working distance objective with a numerical aperture (NA) of 0.42 was used to capture the phase function from a single trapped aerosol,[25,19] while a second camera (C2) coupled to a 10× objective tracked the position of the particle along the full propagation length of the BB. C2 also indicated whether multiple particles were trapped. Aerosol was introduced into the cell via a medical nebuliser (Omron). If multiple particles were trapped, the trapping cell was evacuated and fresh aerosol was nebulised into the cell. This process was repeated until only a single particle was trapped.

Aerosol radii typically have dimensions on the order of the wavelength of visible light. Semi-empirical models cannot describe the angular variation in the light scattering intensity, the phase function (PF), and Mie theory must instead be used. The elastic scattering intensity distribution is affected not only by particle radius but also by the polarisation of the incident light and the refractive index (RI) of the particle, *m*. Here, we denote the real and imaginary components of the RI by *n* and *k* respectively. Measuring the angular variation in the scattered intensity and simulating the measured distribution using Mie theory provides a method of obtaining the particle size even for sub-micron

aerosol particles.[26] This simulation is obtained by computing a library of Mie PFs, comparing each one with the measured PF and performing a least-squares fit. The library of PFs can be computed by floating the variables of particle radius and RI. Typically, for a single measured PF there may be multiple fit solutions with different values of radius for different RI values. Thus, in our measurements, the RI is modelled using literature data and only the radius is fitted.

In addition to the recorded PFs at 532 nm from elastically scattered light from the BB, two further probe beams of different wavelength were employed. The first was from a 35 mW 405 nm diode laser (IQ Series, Power Technology Incorporated) and the second was from a 2 mW 633 nm HeNe laser (LHP073, Melles Griot). These additional probe beams were combined using a polarisation beam splitter (PBS) and aligned anti-parallel to the BB direction. The probe beams were gently focussed into the trapping plane using a 400 mm lens (L5) in order to obtain sufficient scattered light for detection by C1, although their irradiances in the trapping plane were low enough not to affect the particles position and considerably less than that from the trapping 532 nm laser. When collecting PFs from the additional probe beams, various band pass filters were placed between the objective and CCD in C1 to allow collection of light from the respective probe beams and block the more intense 532 nm scattered light from the BB.

III. Measurements of Component Vapour Pressures

Volatilities (vapour pressures) of organic compounds are key thermodynamic properties required for quantifying semi-volatile organic aerosol (SVOA).[27] Vapour pressures can be estimated from single particle measurements by recording the change in radius over time. Glycerol is a good benchmark system to estimate the validity of the BB approach for studying aerosol volatilities; the relatively low hygroscopicity means glycerol absorbs little water, so may be assumed to have a well-defined composition. Numerous glycerol droplets were studied using the BB apparatus, collecting the time-dependent PFs as a droplet was allowed to evaporate. Note that for these experiments, PFs were only collected at 532 nm.

Dry nitrogen was flowed into the trapping cell at a flow rate of 50 sccm until the in-cell RH probe reported a stable, low RH, typically between 5 – 10 %. When an aqueous glycerol solution was nebulised into the cell, the in-cell RH increased rapidly to 25 – 30 % before returning to a stable 5 – 10 % after 6 - 8 minutes. Because of the small size of the droplets (less than 2 μm) and their fast evaporation (under 15 minutes), leaving the measured RH to equilibrate and stabilise at low RH before data acquisition was not possible. However, the low hygroscopicity of glycerol (particularly when compared with inorganic salt systems) suggests the non-zero and varying RH will have a negligible effect on the particle size and evaporation profile. When fitting PFs to Mie theory simulations, the RI was assumed to be constant and equal to the pure component value of $m = 1.475 + i\ 10^{-8}$ over the entire experiment.[28] Maxwell-Garnett and volume-weighting mixing rules show that the difference in the real component of the RI at 0 % and 20 % RH is 0.012, a 0.8 % deviation. This corresponds to a 0.8 % difference in the Mie theory fit radius, which is of a similar magnitude to the uncertainties in PF measurements of radius. Other sources of uncertainty include noise in the PF measurements, not using a precise angular range, and from not using plane wave illumination of the particle, which is a fundamental assumption of Mie scattering theory.

Figure 2(a) shows the radius changes observed for four glycerol particles as they evaporate over time. One measurement is for a coarse mode particle of ~2.9 μm in radius, evaporating to a radius of ~1.7 μm. Further data sets show that fine mode glycerol particles may be trapped and characterised, with one particle evaporating from a radius of ~800 nm to 500 nm. Droplet vapour pressures, p, may be obtained by fitting the Maxwell equation (1) to the time-dependent data.[11]

$$\frac{da^2}{dt} = \frac{2D_{ij}M_i}{R\rho}\left(\frac{p_\infty}{T_\infty} - \frac{p}{T}\right) \qquad (1)$$

D_{ij} is the gas diffusion coefficient of species i in the surrounding phase j, M_i is the molecular weight, a is the particle radius, R is the molar gas coefficient, ρ is the density, p and p_∞ are the vapour pressures at the droplet surface and at infinite distance from the droplet respectively, and T and T_∞ are the corresponding temperatures, assumed to be the same in this case for slow evaporation of low

volatility components. By taking the vapour pressure of component *i* at infinite distance to be negligible and including the effect of non-zero RH, equation (2) can be derived where m_i is the mass fraction of solute *i*.

$$\frac{da^2}{dt} = -\frac{2D_{ij}M_i p}{R\rho T m_i} \qquad (2)$$

Because of non-ideality in the interactions between different species, the pure component vapour pressure, p_0, is related to the measured vapour pressure by $p = p_0 \gamma_i x_i$ where γ_i is the activity coefficient and x_i is the mole fraction of species *i* in the droplet. Hence, by plotting the radius-squared as a function of time, a straight-line fit should be achieved where the gradient is related to p_0. Figure 2(b) summarises the result of measuring 11 pure component vapour pressures in this way, having assumed that both the activity coefficient and the mole fraction of glycerol are equal to unity. The average glycerol vapour pressure is 7.5 ± 2.6 mPa, agreeing satisfactorily with the literature value of 11.6 mPa.[29,28] This level of agreement is quite reasonable when the more significant variations in vapour pressure determinations for components with similar vapour pressures such as dicarboxylic acids are considered.[11] It will now be shown that the wide variation in the measured vapour pressures for glycerol droplets is primarily due to the large variation in the in-cell RH at the beginning of droplet evaporation, and the relatively high volatility of glycerol.

One difficulty in calculating a precise vapour pressure for glycerol is in determining an accurate measure of the RH surrounding the glycerol particles. Nebulising aerosol into the trapping cell causes a large increase in the in-cell RH. Ideally, following nebulisation and particle trapping, the cell would be left for ~20 minutes, passing dry N_2 gas into the cell until the RH stabilises at low (5 – 10 %) RH. 1,2,6-Hexanetriol droplets evaporate more slowly than glycerol, owing to the much lower vapour pressure of the triol and so more accurate measurements of vapour pressure might be expected. Hence, multiple hexanetriol droplets were studied using the BB apparatus. The measurements were performed at an average RH in the range 5 – 10 %, with an RH profile that was more stable than for the previous glycerol studies. Unlike the glycerol experiments, PFs were instead collected at 405 nm

while still employing the 532 nm BB for optical trapping, allowing us to investigate simultaneously the accuracy with which an unknown RI can be determined. Here, we show that the quasi-equilibrium variation in position of hexanetriol droplets along the length of the BB (λ = 532 nm), observed experimentally using camera C2 (Figure 1), can be modelled by Mie theory to obtain both the size evolution of the particle and the RI at 532 nm. Once the size evolution of the particle is determined, the PFs (λ = 405 nm) collected with camera C1 are then fitted, while varying the RI at 405 nm so as to give the same size evolution as given by modelling of the positional data. Thus, these measurements yield simultaneously particle size and refractive index at two wavelengths.

In aerosol optical tweezers, where particles are typically 2 – 10 μm in radius, Raman spectroscopy is used to determine simultaneously radius and refractive index with high accuracy.[25] Whispering gallery modes (WGMs) superimposed on spontaneous Raman bands arise because certain frequencies couple efficiently with the resonant modes of droplet microcavities. However, this method of size determination cannot be employed when probing single particles in the fine mode as there are too few WGMs within the Raman bandwidth for reliable size analysis. A Raman spectrum is a form of *resonance spectrum*, which traditionally describes scattering intensity as a function of the size parameter, the ratio of the circumference of a spherical particle to the incident wavelength. Measuring scattering intensity variation with size at a fixed angle is an alternative method of obtaining a resonance spectrum. For example, Ray and co-workers measured resonances in the scattering intensity for an evaporating glycerol droplet.[30] The position of a confined particle along the length of the core of a BB when subjected to a counter-propagating gas flow is highly dependent on the radiation pressure efficiency of a particle and, as we will show, follows the form of a typical resonance spectrum. Thus, measuring the relative position of an evaporating particle along the length of a BB provides an alternative method of deriving the size evolution of a particle and can be exploited even for sub-micron aerosol particles.

The position of a particle along a single Bessel beam with a counter-propagating gas flow depends on two forces: (i) the force exerted by the laser beam through the action of radiation pressure (F_{pr}); (ii)

247 the Stokes drag force exerted by the gas flow. While the Stokes drag force is simply dependent on the
248 gas flow velocity and particle radius, F_{pr} is more complicated and is proportional to the product of the
249 on-axis core intensity and the radiation pressure efficiency, Q_{pr}, of the particle. The latter term is a
250 measure of how efficiently and asymmetrically a particle scatters light; a particle back-scattering a
251 higher fraction of light has a higher Q_{pr} value.[31] Figure 3(a) shows the variation in position of a
252 hexanetriol particle along the length of the single BB optical trap as a function of evaporation time.
253 The sharp resonances in positional data directly correspond to the resonance structures in Q_{pr} and
254 occur at unique sizes. Hence, only Mie theory simulations of Q_{pr} are required to derive the size
255 evolution of a particle and the effects of Stokes drag and variations in the BB core intensity can be
256 neglected.
257
258 The procedure for comparing positional data with Mie simulations to retrieve droplet size is similar to
259 the fitting of Mie resonance spectra in previous single particle measurements by Chylek *et al.*[32–34] and
260 Ray *et al.*[30,35], and is now briefly described. Q_{pr} is simulated as a function of particle radius and
261 repeated for fixed single values of RI over a range of RIs. Sharp resonance peaks in the Q_{pr}
262 simulations (in the radius domain) can be assigned by matching to peaks in the positional data (which
263 are obtained in the time domain), while also ensuring that the underlying contour reflecting higher
264 order Mie terms is consistent with the data. Plotting these assigned radii against their respective times
265 of observation gives the size evolution of the particle, connecting time, the particle radius, and its
266 position along the length of the BB.
267
268 Figure 3(b) shows the correspondence between the resonant sizes in Q_{pr} and the resonant excursions
269 in the particle position along the length of the BB. Differences in the signal amplitude between the
270 positional data and the Q_{pr} simulations are likely because the effects of Stokes drag and variations in
271 the core intensity with propagation have been neglected. It can be seen in Figure 3(b) that the
272 positions of resonance peaks in the position data do not agree exactly with the positions of resonance
273 peaks in the Q_{pr} simulation. The residual differences between the positions of resonance peaks in the

Mie simulation ($a_{i,sim}$) and the experimental measurement ($a_{i,\exp}$) provide a measure of the agreement between the simulation (for a given RI) and the position measurements. The total residual of a fit, D_{fit}, is given by equation (3).

$$D_{fit} = \sum_i \left| a_{i,\exp} - a_{i,sim} \right| \qquad (3)$$

Repeating this procedure and obtaining the fit residuals for simulations using different RIs allows a determination of the RI at 532 nm. This outcome is demonstrated in Figure 3(c) for three studies, which indicate an RI of 1.482 ± 0.001 at 532 nm. Refractometer measurements give a bulk refractive index of 1.4758 at a wavelength of 589.6 nm. A higher refractive index at a lower wavelength is expected, given typical trends in dispersion for other materials. No literature data at the wavelength of 532 nm can be found.

Figure 4(a) shows how the radii evolve with time for five droplets, with droplet sizes determined from their positional data as well as from their 405 nm PF data. When performing the PF analysis, the RI at 405 nm was adjusted until only the initial radius (i.e. the radius at t = 0 s) matched that given from modelling the positional data. Subsequent trends during evaporation illustrate the consistency that is then obtained between the two size-determination methods at the two wavelengths. Assuming the imaginary component of the RI, k, to be equal to 10^{-8}, the real component, n, at 405 nm was consistently determined to be 1.485 ± 0.006 from measurements on multiple droplets. Again, no literature value of RI can be found specifically at the wavelength of 405 nm which to compare our measured value. The three real RIs now obtained for hexanetriol (1.485 at 405 nm, 1.482 at 532 nm, 1.476 at 589.6 nm) can be fitted to refractive index models such as Cauchy's equation. RI's at further wavelengths are required to quantitatively assess the accuracy of such models in describing the dispersion in the RI of hexanetriol. The possibility of retrieving a more detailed wavelength dependence of RI will feature in future work.

The five hexanetriol droplets remained optically trapped for much longer than glycerol droplets, with one droplet isolated for 10 hours. As experiments were performed at a low RH of ~5 %, the mass

fraction of water in the droplets is assumed to be negligible and the activity coefficient of hexanetriol is taken to be unity. Figure 4(b) shows calculated vapour pressures for five droplets with an average value of 0.20 ± 0.02 mPa. The 10% variation in the measured hexanetriol p_0 compared to the 35% variation for glycerol demonstrates that greater reproducibility can be achieved in vapour pressure measurements when the in-cell RH can be well defined. No comment can be made on the accuracy of our measurement of p_0 for hexanetriol as there are no current literature values for this compound with which to compare.

IV. Hygroscopic Growth Measurements

Hygroscopicity studies require measurements of the changes in the equilibrium partitioning of water between the gas and particle phases with variation in RH, most often through measurements of relative size.[11] Due to non-ideal interaction of water with solutes, thermodynamic models are required to describe the activity coefficients of solutions, particularly for the supersaturated droplets probed in aerosol systems. Here, we compare hygroscopic growth measurements of involatile inorganic salt systems to simulations of growth from the Extended Aerosol Inorganic Model (E-AIM), an equilibrium state model which can describe the relationship between particle growth and changes in the RH.[36] Vapour pressure and hygroscopicity measurements aid in the parameterisation and validation of such thermodynamic models.[11]

As an aerosol particle takes up water with an increase in RH, both the RI and size of the particle change. Fitting the PFs obtained from binary component droplets (water and solute) in hygroscopicity experiments is more complicated than fitting those from vapour pressure experiments and it is not possible to retrieve both the RI and size from a single PF, with several solution combinations of RI and particle radius possible. Instead, the RI has to be described as a function of particle radius, *a*. For a binary system with volume fractions φ_1 and φ_2 for pure water and pure solute, respectively, the linear volume-fraction average mixing rule is often encountered in studies of aerosols. However, this treatment of refractive index is not applicable in many cases, as shown by Liu and Daum.[37] Thus, we

have opted to use the parameterisations of Tang and Munkelwitz[38] for various inorganic aerosol systems, which is now briefly described. The real component of the RI, *n*, for a binary aerosol can be modelled in terms of particle radius, *a*, using equation (4).

$$n = n_w + gc_2 + hc_2^{\,2} = n_w + g\left[\frac{a_0^{\,3}c_{2,0}}{a^3}\right] + h\left[\frac{a_0^{\,3}c_{2,0}}{a^3}\right]^2 \qquad (4)$$

n_w is the real component of RI for pure water, c_2 is the solute concentration, and a_0 is the particle radius at some reference concentration of solute $c_{2,0}$. Tang and Munkelwitz[38] reported the RIs at 633 nm of several aqueous inorganic aerosols and their dependence on the solute concentration, c_2. Using their parameterisations, the constants *g* and *h* in equation (4) may be calculated for a particular inorganic species. Figure 5 shows the variation of n with c_2 for both a sodium chloride and an ammonium sulphate aerosol, as determined by Tang and Munkelwitz. A polynomial fit to their parameterisation gives the constants *g* and *h*. A small wavelength correction is also applied to the RI to account for dispersion; we use the correction given by Millard and Seaver.[39] The parameters $c_{2,0}$ and a_0 remain to be determined. The E-AIM model can relate RH to solute concentration, so using the measurement of the in-cell RH (which has a ±2% accuracy) E-AIM is used to determine the solute concentration $c_{2,0}$ at a reference RH (usually taken to be the RH at t = 0 s). Subsequently, equation (4) is used to determine the RI of the initial droplet at $c_{2,0}$. The PF recorded at this reference RH is then fitted using this value of RI to determine a_0. A library of phase functions can now be generated in the same way as in previous PF analyses, except that the RI is varied with radius in the form given by equation (5), as opposed to having a constant value.

Aqueous sodium chloride droplets were nebulised into the optical trapping cell and the initial RH was kept high (between 85 – 95 %). The laser power was set at powers in the range 1 – 2 W, corresponding to core intensities in the range 0.3 - 0.6 mW μm^{-2}. After an equilibration time of ~20 minutes, the RH was lowered to 30-40% over 1 hour, during which time the particle axial positions along the propagation distance and the PFs at 532 nm were recorded. The changes in RH are

sufficiently slow that the droplet is always at equilibrium during measurement and, thus, water transport kinetics can be neglected. An example data set is shown in Figure 6(a). As expected, the particle radius decreases as the in-cell RH is reduced and effloresces in the region 37 – 41 % RH (for comparison, literature values range from 39 to 54% RH).[11] Unlike in optical tweezers experiments, the effloresced particle remains stably trapped. Predictions of the radial growth factor (RGF) calculated from the E-AIM model can be compared to the pre-efflorescence data. The RGF is the ratio of the particle radius to its radius at 0% RH (dry radius). E-AIM calculations of RGF were fitted to the experimental data using a least-squares method and floating the dry radius parameter. The distribution of normalised least-squares residuals with dry radius can be fitted to a Gaussian distribution, from which an uncertainty in the dry radius can be obtained. This uncertainty is shown in Figure 6(a) by the shaded grey area. The experimental pre-efflorescence data show good agreement with E-AIM, and the dry radius obtained by the fit is indicated by the dashed red line.

Interestingly, the PFs from the supposedly crystalline NaCl particle closely resemble those expected from a sphere, with distinct dark and bright fringes, although they were observed to 'shimmer' at times with bright fringes appearing broken in a regular pattern. The fact that a PF resembling a spherical particle is obtained may suggest that the effloresced NaCl particle has not adopted the expected equilibrium cubic structure immediately. Modelling post-efflorescence PFs with Mie theory gives dry particle radii very close to the values expected from the E-AIM fit to the pre-efflorescence data. This is shown by the experimental data points in Figure 6(a) distributed just below the dashed red line, implying the PFs obtained are indeed for an effloresced NaCl particle but for a period during which the effloresced particle remains approximately spherical. Although effloresced NaCl particles are generally assumed to have a cubic shape, nearly spherical NaCl particles have been observed by others in the literature.[40]

Further information is given by the particle position data along the propagation length of the BB (Figure 6(b)). The pattern of periodic resonances expected for a particle that is changing size ends after efflorescence, as marked in the figure by the label 'crystallisation'. However, position

fluctuations continue following efflorescence, but are seemingly random in nature. The reason for these fluctuations is unclear. One possibility is that the effloresced particle is not completely crystalline and initially retains at least some of the solution phase. This structure may be evolving over time, tending towards the equilibrium cubic structure of NaCl as further residual water evaporates from the particle. Such structural changes will impact on the optical properties and radiation pressure efficiency of a particle, affecting its position along the length of the BB. Instantaneous fluctuations in the orientation of the particle in the optical trap as it tumbles, if non-spherical, can also lead to large and rapid deviations in particle position as the magnitude of the radiation pressure changes.

So far, the particles studied are far larger than the fine mode particles we wish to probe using Bessel beams. Carruthers and co-workers showed that the size range of particles isolated using BB optical traps can be preferentially selected by changing the BB core diameter.[19] Thus, reducing the core diameter should favour the trapping of smaller particles. The post-axicon BB core diameter was 55.5 $\pm$ 2.9 μm and may be tuned in the optical trapping region by tweaking the focal length ratio of lenses L3 to L4 in Figure 1. The lens ratio L3/L4 was increased to 20 from the value of 12.5 used so far, resulting in the measured core diameter decreasing from 4.7 $\pm$ 0.3 μm to 2.6 $\pm$ 0.1 μm. Also, the solute concentration in the nebuliser can be reduced so as to produce a size distribution of nebulised aerosol peaking at smaller size. Subsequent hygroscopicity studies performed on aqueous NaCl droplets clearly showed the trapping and reliable sizing of NaCl droplets down to radii of 600 nm, with the hygroscopic growth curves again broadly consistent with predictions from E-AIM. Smaller particles were optically trapped, but their PFs recorded at 532 nm were featureless so the particles could not be sized.

In an attempt to size aerosol truly within the fine mode reliably, use of a lower (visible) probe wavelength is logical. To this end, the 35 mW 405 nm probe beam (alignment as shown in Figure 1) was used to collect PFs. Figure 7 shows an example of a hygroscopicity measurement for an aqueous

NaCl droplet, using the 405 nm probe beam to determine the radius for a droplet which could not be reliably sized using the 532 nm beam. The figure also shows the corresponding PFs at 405 nm and 532 nm for the droplet at t = 0 s (corresponding to 80 % RH). The 405 nm PF clearly has features which can be used to fit to Mie theory simulations, whereas the 532 nm PFs are completely featureless (neglecting the side peaks from optical aberrations). The radius of the droplet was determined to be 510 nm from the PF at the probe wavelength of 405 nm. Droplets have been reliably sized down to radii of ~350 nm, well into the fine mode regime relevant to atmospheric chemistry and physics. These results represent the smallest single-particle measurements of hygroscopicity made. Indeed, particles around this size present the largest total optical cross-section to visible light in the atmosphere, with large geometric cross-section, extinction and scattering efficiency and sufficient number density.

Ammonium sulfate is another atmospherically-relevant aerosol system and hygroscopicity measurements have been performed using the BB apparatus, measuring PFs using the 405 nm probe beam. A summary plot, averaging the RGF from hygroscopic growth measurements of seven accumulation mode droplets (<500 nm in radius), is presented in Figure 8(a). Errors are calculated by taking the standard deviation in the RGF values, and assuming a ± 2 % standard error in the measured RH. Figure 8(b) also shows a summary of seven studies on sodium chloride accumulation mode particles. Evidently, for both ammonium sulfate and sodium chloride, the hygroscopic growth of accumulation mode particles is well described by E-AIM.

V. Conclusions

The capability of BB optical traps to measure the vapour pressure and hygroscopicities of fine and accumulation mode aerosol has been successfully demonstrated. Vapour pressures of organic aerosol have been measured, with a demonstrated reproducibility within 16 % precision if the optical trapping cell RH can be well defined and maintained over the entire course of the experiment. A first attempt has been presented to model the position of particles subjected to radiation pressure from the BB and

a counter-propagating gas flow. Analysis of the sharp resonances in particle position data determines both the size evolution of hexanetriol particles and the RI at 532 nm. The accuracy of the RI value obtained is limited by the resolution of the position of the particle along the length of the beam. This uncertainty can be reduced by using a longer BB core length and by reducing the exposure on the camera recording the particle position giving higher time resolution of particle position. The size evolution of the particle from position data agrees with that determined by analysis of PFs recorded using a 405 nm probe beam. This agreement is only achieved when using a fixed real component of the RI at 405 nm of 1.485 ± 0.006. Future work will involve repeating measurements for further probe beam wavelengths (e.g. 633 nm) to see how well dispersion models describe the wavelength dependence of the RI of hexanetriol.

Hygroscopicity measurements on sodium chloride and ammonium sulfate aerosols have been performed for particles as small as 350 nm in radius. These results represent the first single-particle measurements of hygroscopicity on fine mode and accumulation mode aerosols, the size regime which has the most atmospheric significance in terms of loading and light extinction/scattering efficiencies. The variation in radial growth factor with RH agrees well with the results from the E-AIM thermodynamic models. There are two principal factors that raise questions over the reliability of our measurements. Firstly, the RH within the cell is poorly defined with a precision of ± 2 % at best. It is further assumed that the in-cell RH measured by a probe near to the wall of the cell is the same as that experienced by an optically trapped particle at the centre of the trapping cell. We have attempted to ensure that this is true by positioning the RH probe as close to the trapping region as possible given the physical constraints of the trapping cell. If the probe is saturated there could be a delay in equilibration of the probe with the environment of the rest of the cell. Secondly, the fitting of PFs relies on having an accurate description of the RI and assumes a dependence on radius. Although the parameterisations of Tang and Munkelwitz[38] are commonly used to describe RI as a function of concentration, we have to use our measurements of RH to obtain the starting droplet concentration, which suffers from an uncertainty of ± 2 %. Further, Tang and Munkelwitz's parameterisations are

valid at 633 nm only. So, when describing the RI of sodium chloride or ammonium sulfate for PFs recorded from a 405 nm probe beam, a dispersion model formulated for sea salt aerosol is applied.[39] However, such dispersion models may not be valid over such large wavelength ranges.

EDB techniques are now at a point at which the RH of the trapping cell can be defined to better than 0.2 %.[4] However, EDB methods also employ PF analysis to extract size information so they still rely on modelling the RI. As well as being able to extract aerosol radius to a precision better than 1 nm, optical tweezers methods employing Raman spectroscopy can simultaneously measure the RI with an uncertainty better than 0.1 %, and can quantify the dispersion over a narrow wavelength range.[12] However, RH measurements are performed by capacitance probe methods so suffer the same level of uncertainty as our measurements. Thus, to exploit the high level of accuracy in quantifying droplet size and RI in such measurements, comparative measurements on multiple droplets must be performed.[41] Indeed, we have shown here that the uncertainty with which hygroscopic growth measurements can be made on fine mode inorganic aerosol using the BB optical trapping approach (± 3% error in RGF for a given RH) is comparable to the typical uncertainty associated with ensemble accumulation mode measurements made using the hygroscopic tandem differential mobility analysis technique, typically ± 3% for inorganic aerosol as seen in Figure 1 of reference [42] with errors in RH that are also similar.

Acknowledgements

JPR, AJOE and AEC acknowledge financial support from the EPSRC through the support of a Leadership Fellowship (EP/G007713/1) awarded to JPR. MIC acknowledges funding from NERC and the RSC through an Analytical Trust Fund studentship award and support from the Aerosol Society in the form of a CN Davies award. BJM and JSW acknowledge the EPSRC for funding. We also acknowledge Thomas C. Preston for helpful discussions.

References

1. S. Solomon, D. Qin, M. Manning, M. Marquis, K. Averyt, M. M. B. Tignor, J. Miller, Henry LeRoy, and Z. Chen, *Climate Change 2007: The Physical Science Basis - Contribution of Working Group I to the Fourth Assessment Report of the Intergovernmental Panel on Climate Change*, 2007.

2. G. McFiggans, et al., *Atmos. Chem. Phys.*, 2006, **6**, 2593–2649.

3. J. Julin, M. Shiraiwa, R. E. H. Miles, J. P. Reid, U. Pöschl, and I. Riipinen, *The Journal of Physical Chemistry A*, 2013, **117**, 410–20.

4. J. F. Davies, A. E. Haddrell, A. M. J. Rickards, and J. P. Reid, *Anal. Chem.*, 2013, **85**, 5819–5826.

5. D. A. Hegg, D. S. Covert, K. K. Crahan, H. H. Jonsson, and Y. Liu, *Geophysical Research Letters*, 2006, **33**, L21808.

6. B. J. Mason, S.-J. King, R. E. H. Miles, K. M. Manfred, A. M. J. Rickards, J. Kim, J. P. Reid, and A. J. Orr-Ewing, *The Journal of Physical Chemistry. A*, 2012, **116**, 8547–8556.

7. A. R. Attwood and M. E. Greenslade, *The Journal of Physical Chemistry A*, 2012, **116**, 4518–4527.

8. D. Topping, P. Connolly, and G. McFiggans, *Nature Geoscience*, 2013, **6**, 443–446.

9. J. F. Davies, A. E. Haddrell, and J. P. Reid, *Aerosol Science and Technology*, 2012, **46**, 37–41.

10. F. D. Pope, H. Tong, B. J. Dennis-smither, P. T. Griffiths, S. L. Clegg, J. P. Reid, and R. A. Cox, *The Journal of Physical Chemistry A*, 2010, **114**, 10156–10165.

11. U. K. Krieger, C. Marcolli, and J. P. Reid, *Chemical Society Reviews*, 2012, **41**, 6631–62.

12. R. E. H. Miles, J. S. Walker, D. R. Burnham, and J. P. Reid, *Physical Chemistry Chemical Physics*, 2012, **14**, 3037–47.

13. B. J. Dennis-Smither, K. L. Hanford, N.-O. A. Kwamena, R. E. H. Miles, and J. P. Reid, *The Journal of Physical Chemistry. A*, 2012, **116**, 6159–68.

14. R. M. Power, S. H. Simpson, J. P. Reid, and A. J. Hudson, *Chemical Science*, 2013, **4**, 2597–2604.

15. E. R. Lewis, *Journal of Aerosol Science*, 2006, **37**, 1605–1617.

16. J. Durnin, *Journal of the Optical Society of America A*, 1987, **4**, 651–654.

17. J. Durnin and J. J. Miceli, *Physical Review Letters*, 1987, **58**, 1499–1501.

18. A. E. Carruthers, J. P. Reid, and A. J. Orr-Ewing, *Optics Express*, 2010, **18**, 14238–44.

19. A. E. Carruthers, J. S. Walker, A. Casey, A. J. Orr-Ewing, and J. P. Reid, *Phys. Chem. Chem. Phys.*, 2012, **14**, 6741–6748.

20. J. S. Walker, A. E. Carruthers, A. J. Orr-Ewing, and J. P. Reid, *The Journal of Physical Chemistry Letters*, 2013, **4**, 1748–1752.

21. D. McGloin and K. Dholakia, *Contemporary Physics*, 2005, **46**, 15–28.

22. M. Duocastella and C. B. Arnold, *Laser & Photonics Reviews*, 2012, **6**, 607–621.

23. J. Jezek, T. Cizmár, V. Nedela, and P. Zemánek, *Optics express*, 2006, **14**, 8506–15.

24. M. Mazilu, D. J. Stevenson, F. Gunn-Moore, and K. Dholakia, *Laser & Photonics Reviews*, 2009, **4**, 529–547.

25. R. E. H. Miles, A. E. Carruthers, and J. P. Reid, *Laser & Photonics Reviews*, 2011, **5**, 534–552.

26. J. P. Reid and L. Mitchem, *Annual Review of Physical Chemistry*, 2006, **57**, 245–71.

27. I. Riipinen, I. K. Koponen, A. Hyva, J. Vanhanen, H. Lihavainen, K. E. J. Lehtinen, M. Bilde, and M. Kulmala, *The Journal of Physical Chemistry. A*, 2007, **111**, 12995–13002.

28. H. K. Cammenga, F. W. Schulze, and W. Theuerl, *Journal of Chemical and Engineering Data*, 1977, **22**, 131–134.

29. J. F. Davies, A. E. Haddrell, and J. P. Reid, *Aerosol Science and Technology*, 2012, **46**, 666–677.

30. A. K. Ray, R. Johnson, and A. Souyri, *Langmuir*, 1989, **5**, 133–140.

31. W. M. Irvine, *Journal of the Optical Society of America*, 1965, **55**, 16–21.

32. P. Chýlek, *Journal of the Optical Society of America*, 1976, **66**, 285–287.

33. P. Chylek, J. T. Kiehl, and M. K. W. Ko, *Physical Review A*, 1978, **18**, 2229–2233.

34. P. Chylek, V. Ramaswamy, A. Ashkin, and J. M. Dziedzic, *Applied Optics*, 1983, **22**, 2302–2307.

35. A. K. Ray, A. Souyri, E. J. Davis, and T. M. Allen, *Applied Optics*, 1991, **30**, 3974–3983.

36. S. L. Clegg, P. Brimblecombe, and A. S. Wexler, *The Journal of Physical Chemistry A*, 1998, **102**, 2155–2171.

37. Y. Liu and P. H. Daum, *Journal of Aerosol Science*, 2008, **39**, 974–986.

38. I. N. Tang and H. R. Munkelwitz, *Journal of Geophysical Research*, 1994, 18801–18808.

39. R. C. Millard and G. Seaver, *Deep-Sea Research*, 1990, **37**, 1909–1926.

40. A. Zelenyuk, Y. Cai, and D. Imre, *Aerosol Science and Technology*, 2006, **40**, 197–217.

41. J. S. Walker, J. B. Wills, J. P. Reid, L. Wang, D. O. Topping, J. R. Butler, and Y.-H. Zhang, *The Journal of Physical Chemistry. A*, 2010, **114**, 12682–91.

42. N. Good, D. O. Topping, J. Duplissy, M. Gysel, N. K. Meyer, A. Metzger, S. F. Turner, U. Baltensperger, Z. Ristovski, E. Weingartner, H. Coe, and G. McFiggans, *Atmospheric Chemistry and Physics Discussions*, 2010, **10**, 2577–2593.

Figure 1 – Schematic of the apparatus used to generate a Bessel beam and optically trap single aerosol particles. C1 and C2 represent 'camera 1' and 'camera 2' respectively, PBS is a 'polarisation beam splitter', and L1-L5 represent lenses.

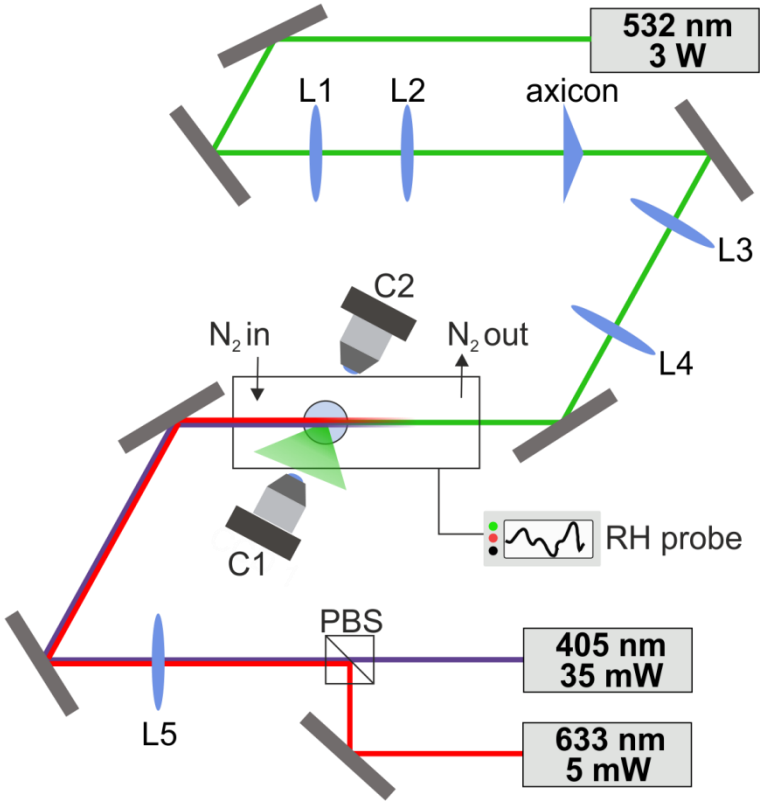

Figure 2 - (a) Four data sets measuring the radius as a function of time for optically-trapped glycerol droplets as they evaporate at an RH of ~15-20 %. (b) Vapour pressures from eleven studies give an average p_0 of 7.5±2.6 mPa. The crosses indicate individual measurements and the circle and error bar indicate the mean and standard deviation.

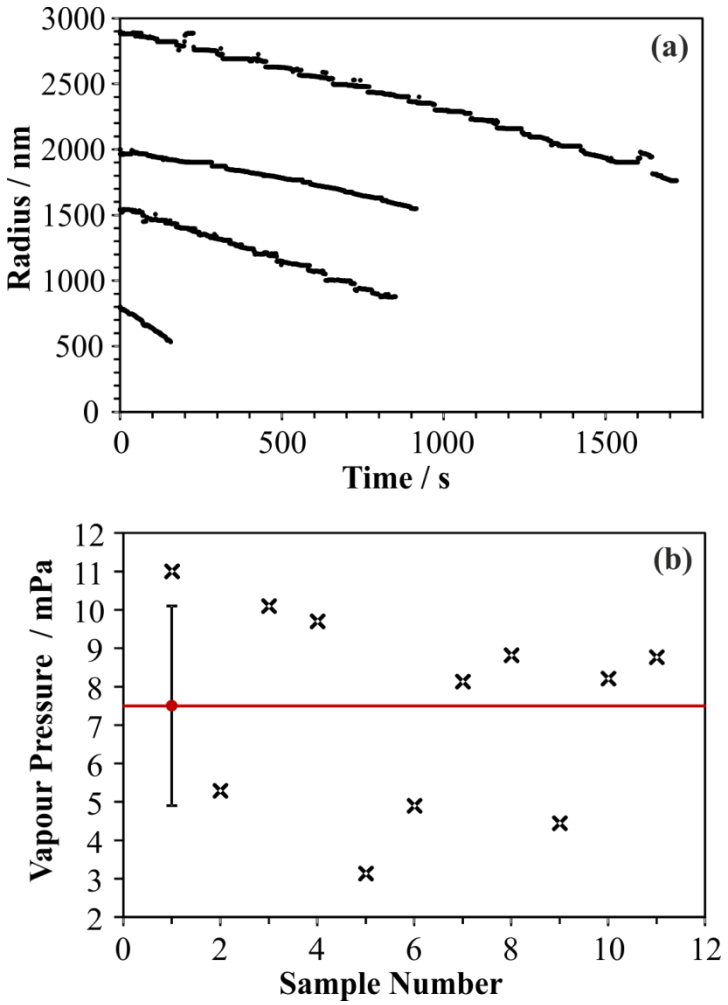

Figure 3 – (a) Measured position of the hexanetriol droplet in Study 1 along the length of a Bessel beam as it evaporates over time. (b) Measured position data from Study 1 (black) in the radius domain, accompanied by the best fit simulation of Q_{pr} (red) which used a real component of the RI of 1.483. (c) Normalised residual in Q_{pr} fits as a function of RI at 532 nm for three different studies. Lines between data points are to guide the eye only.

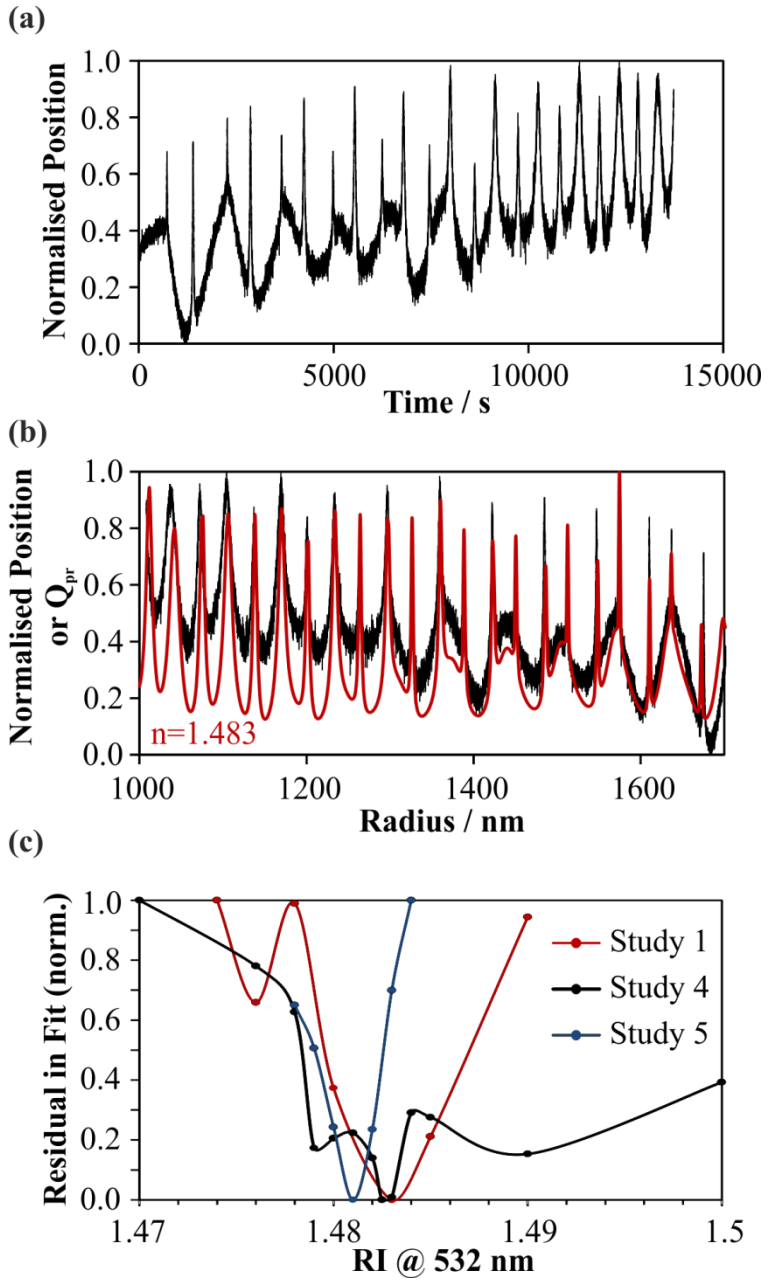

574 **Figure 4 - (a) Five hexanetriol studies measuring the radius as a function of time using position data (red) and**
575 **subsequent measurement from phase function data (black). (b) Vapour pressures from five hexanetriol studies give**
576 **an average p_0 of 0.20 ± 0.02 mPa.**

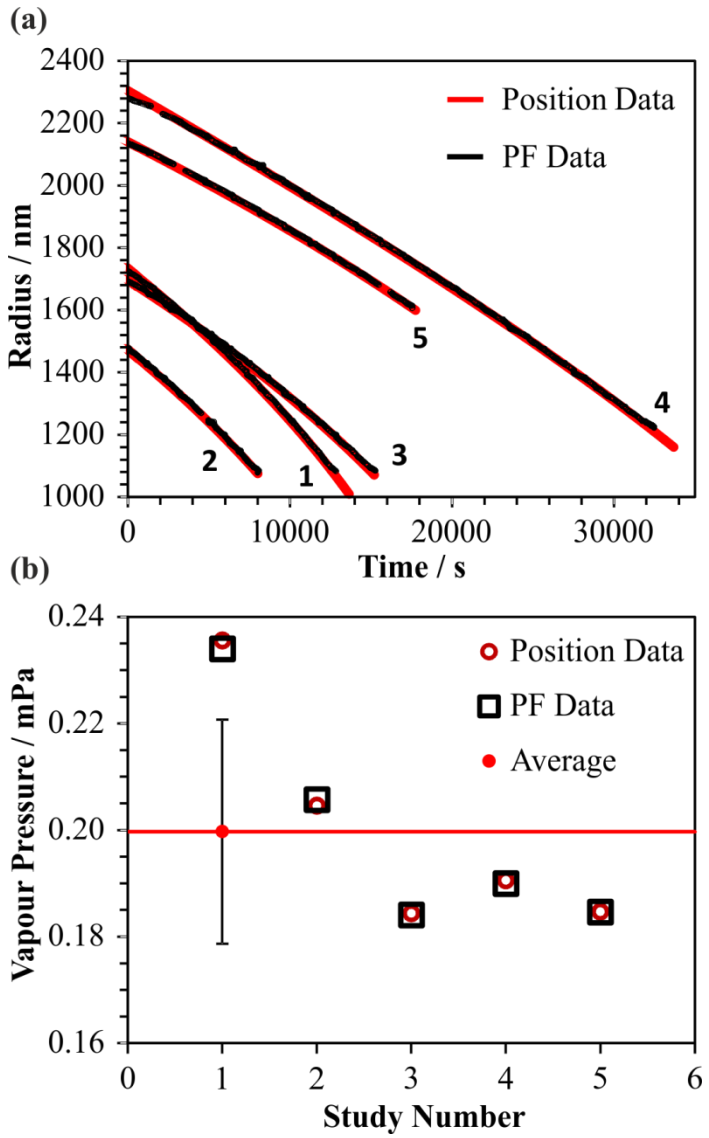

577
578

Figure 5 – The calculated variation in the real component of refractive index, *n*, with solute concentration, c_2, using the parameterisations of Tang and Munkelwitz.[38] Black dots show data points, while the red line is a second-order polynomial fit to data points, the equation for which is given.

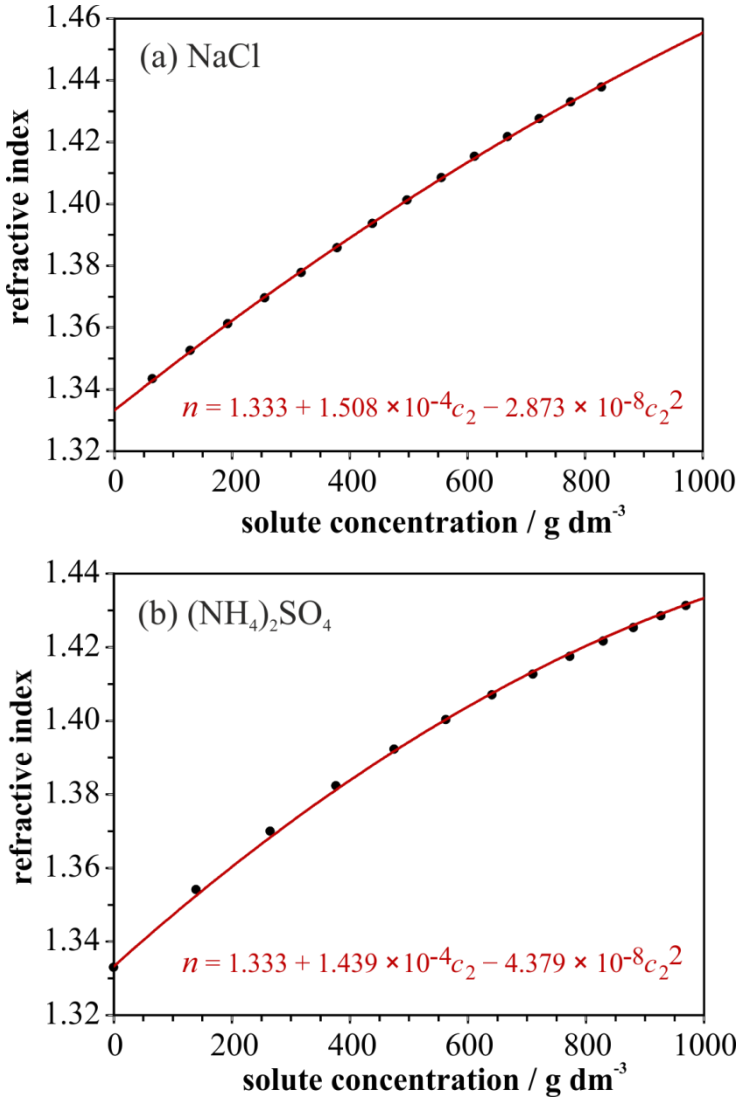

Figure 6 – (a) An example NaCl hygroscopicity data set using a 4.7 µm core diameter Bessel beam. Experimental data points shown by black dots, accompanied by a comparison to the E-AIM model (red line) which has an associated uncertainty (shaded grey area). Dashed red line indicates the dry radius estimated from a fit of E-AIM model to experimental data points. Typical uncertainty in relative humidity is ± 2%. (b) The particle position along the Bessel beam length for the data set in (a).

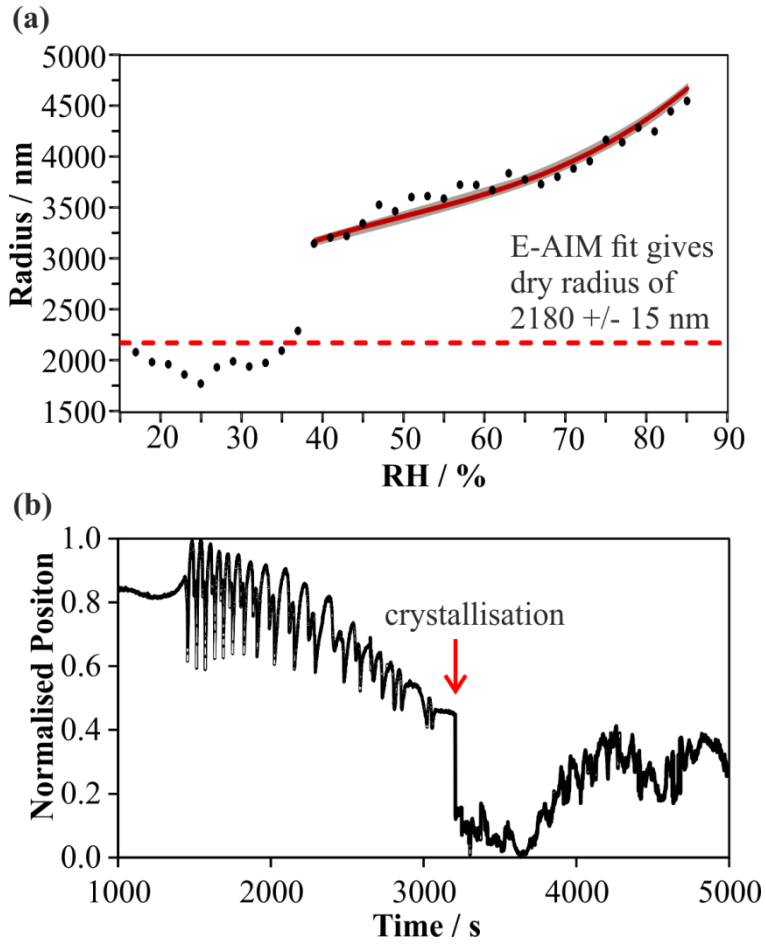

Figure 7 – (a) Example hygroscopicity study on an aqueous NaCl aerosol droplet in the accumulation mode regime, with the radius determined from 405 nm phase functions. (b) Phase functions at probe wavelengths 405 nm (blue line) and 532 nm (green line) for the initial droplet in (a) at high relative humidity. Inset are the raw phase function images at 405 nm and 532 nm.

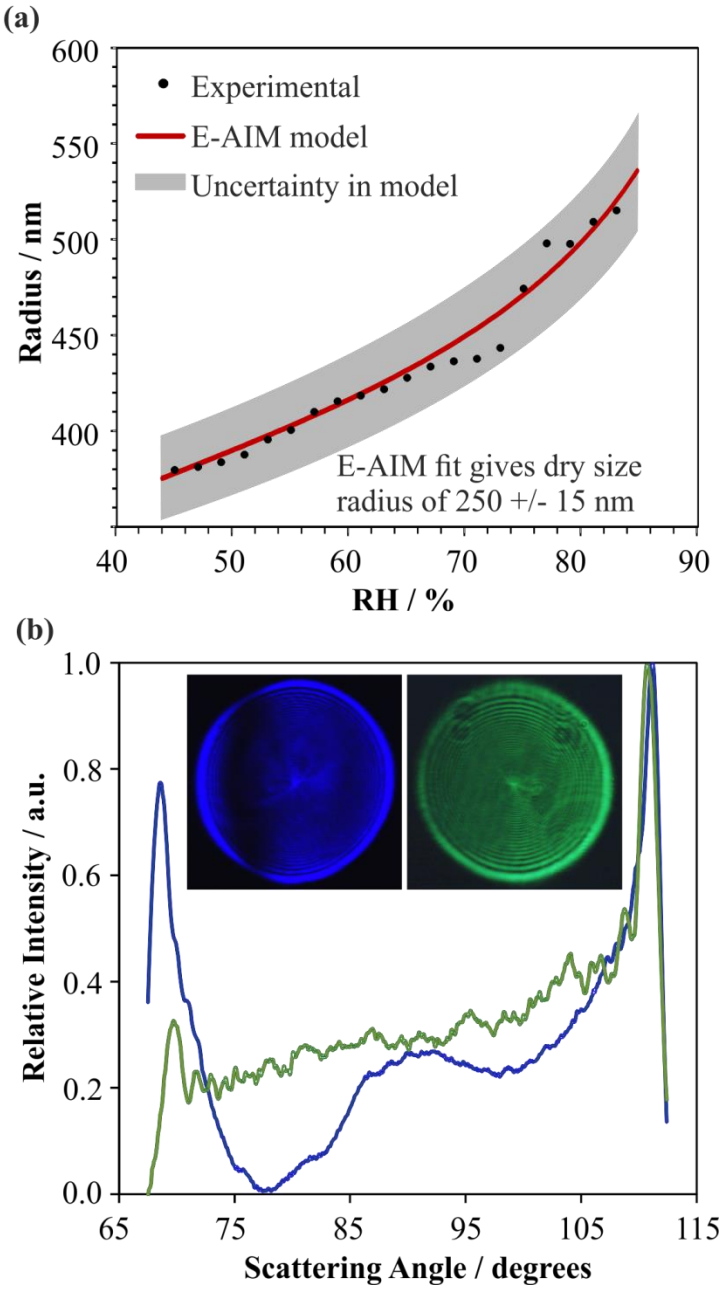

598 **Figure 8 – Summary of hygroscopic growth measurements on: (a) ammonium sulfate; (b) sodium chloride. In each**
599 **case, the radial growth factor is an average from seven hygroscopic growth measurements on accumulation mode**
600 **(<500 nm radius) aerosol particles.**

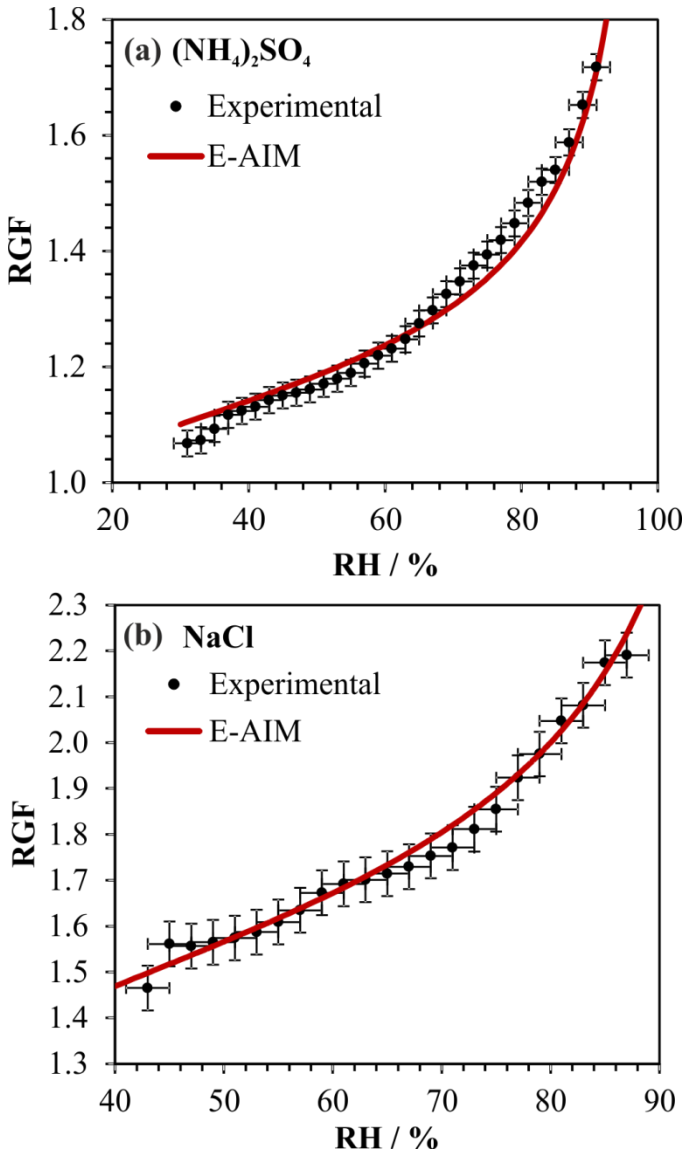

601